# Relative Permeability Variation Depending on Viscosity Ratio and Capillary Number

**Natanael Suwandi[1], Fei Jiang[2,3], Takeshi Tsuji[1,2,4]**

[1]Department of Cooperative Program for Resources Engineering, Graduate School of Engineering, Kyushu University, Fukuoka 819-0395, Japan

[2]International Institute for Carbon-Neutral Energy Research, Kyushu University, Fukuoka 819-0395, Japan

[3]Department of Mechanical Engineering, Graduate School of Sciences and Technology for Innovation, Yamaguchi University, Yamaguchi 755-8611, Japan

[4]Department of Earth Resources Engineering, Faculty of Engineering, Kyushu University, Fukuoka 819-0395, Japan

Corresponding author: Takeshi Tsuji (tsuji@mine.kyushu-u.ac.jp)

**Key Points:**

- Relative permeability in two-phase flow is calculated in a three-dimensional digital Berea rock using Lattice Boltzmann Method
- Relative permeability varies due to lubrication effect, shear force and capillary force, and is related to fluid droplet fragmentation
- Relative permeability on viscosity ratio-capillary number map is created to predict spatiotemporal variation of reservoir permeability

## Abstract

The relative roles of parameters governing relative permeability, a crucial property for two-phase fluid flows, are incompletely known. To characterize the influence of viscosity ratio ($M$) and capillary number ($Ca$), we calculated relative permeabilities of nonwetting fluids ($k_{\mathrm{nw}}$) and wetting fluids ($k_{\mathrm{w}}$) in a 3D model of Berea sandstone under steady-state condition using the lattice Boltzmann method. We show that $k_{\mathrm{nw}}$ increases and $k_{\mathrm{w}}$ decreases as $M$ increases due to the lubricating effect, locally occurred pore-filling behavior, and instability at fluid interfaces. We also show that $k_{\mathrm{nw}}$ decreases markedly at low $Ca$ ($\log Ca < -1.25$), whereas $k_{\mathrm{w}}$ undergoes negligible change with changing $Ca$. An $M$–$Ca$–$k_{\mathrm{nw}}$ correlation diagram, displaying the simultaneous effects of $M$ and $Ca$, shows that they cause $k_{\mathrm{nw}}$ to vary by an order of magnitude. The color map produced is useful to provide accurate estimates of $k_{\mathrm{nw}}$ in reservoir-scale simulations and to help identify the optimum properties of the immiscible fluids to be used in a geologic reservoir.

## Plain Language Summary

The relative permeability is a crucial parameter in a system where two fluid phases exist simultaneously. For example, in carbon capture and storage, relative permeability is important to assess the replacement mechanism of the existing fluid in the reservoir (wetting fluid) by the injected $CO_2$ (non-wetting fluid). It is also an important parameter in enhanced oil recovery fields, as high relative permeability of oil indicates that the oil in the reservoir can be extracted quickly. The relative permeability is temporally and spatially varied by reservoir conditions (e.g., temperature). But currently, in reservoir-scale fluid flow simulation, relative permeability is assumed to be constant regardless of the different conditions. In this study, we conducted simulations to calculate relative permeability in various viscosity ratio (*M*) and capillary number (*Ca*) conditions. We found that relative permeability changes dramatically in different *M* and *Ca* conditions, and we further mapped relative permeability on the diagram between *M* and *Ca* to predict relative permeability accurately in various reservoir conditions. Our findings can be useful to determine the suitable fluid properties to be used in reservoir management and to accurately estimate fluid behavior based on reservoir-scale simulation with variant relative permeability.

## 1 Introduction

The relative permeability of the different fluids in a two-phase flow has been extensively studied in scientific and engineering fields concerned with two-phase flows in geological reservoirs, such as in carbon capture and storage (CCS) fields, enhanced oil recovery (EOR) operations, geothermal power systems, and geological radioactive waste disposal repositories (Benson et al., 2015; C. Chen & Zhang, 2010; Gudjonsdottir et al., 2015; Niibori et al., 2011; Shad et al., 2008; Wu & Wang, 2020). Relative permeability is a crucial hydraulic property for modeling the flow of both fluids and assessing the mechanisms of fluid displacement in the reservoir. For example, when $CO_2$ is injected into a CCS reservoir, the $CO_2$ (nonwetting phase) displaces the existing fluid in the reservoir, such as oil or brine (wetting phase). Relative permeability values can be used to estimate the reduction in $CO_2$ fluid flow due to surface-tension effects between $CO_2$ and the brine, thus the parameter is useful to assess the injectivity of the $CO_2$ (Benson et al., 2015; Burnside & Naylor, 2014). The relative permeability can also aid estimation of how much fluid can be displaced by $CO_2$ before the system reaches the wetting fluid irreducible saturation condition, limiting the $CO_2$ volume that can be stored in the reservoir

(Burnside & Naylor, 2014). Conversely, in EOR systems, the best results are obtained when the relative permeability is high for oil and low for the injected fluid (Heins et al., 2014).

Several factors influence relative permeability in a two-phase flow system. For example, in a CCS project, the fluid relative permeability is affected by the heterogeneity of the rock, such as pore size and pore connectivity (Benson et al., 2015; Fei Jiang & Tsuji, 2014; Zhang et al., 2022). In addition, relative permeability is affected by the interactions between the two fluids, such as interfacial tension, the viscosity and velocity of the fluids, and their wettability (Lefebvre du Prey, 1973). Because fluid viscosity varies dramatically with pressure and temperature, such reservoir environments can further affect relative permeability. Therefore, in a two-phase flow system, the relative permeability value of each fluid is not only a function of saturation; it is also affected by other parameters related to environmental and by the interaction between the two component fluids.

Lenormand et al. (1988) reported that two parameters, viscosity ratio and capillary number, can explain the interaction between two immiscible fluids. The viscosity ratio (*M*) is a dimensionless parameter describing the ratio between the viscosity of the injected nonwetting fluid and the viscosity of the ambient wetting fluid:

$$M = \frac{\mu_{\mathrm{nw}}}{\mu_{\mathrm{w}}} \qquad (1)$$

where $\mu_{\mathrm{nw}}$ is the dynamic viscosity of the nonwetting fluid and $\mu_{\mathrm{w}}$ is the dynamic viscosity of the wetting fluid.

The capillary number (*Ca*) is a dimensionless parameter describing the ratio between the viscous drag forces and the interfacial tension forces between two immiscible fluids:

$$Ca = \frac{\mu_{\mathrm{nw}} V_{\mathrm{nw}}}{\sigma} \qquad (2)$$

where $V_{\mathrm{nw}}$ is the average fluid velocity of the nonwetting fluid and $\sigma$ is the interfacial tension (IFT) between the two fluids.

Despite the recognition that the relative permeability $k$ is a function of $M$, several studies of this relationship have reported divergent results. An experimental study (Odeh, 1959) found that the relative permeability of the nonwetting fluid ($k_{\mathrm{nw}}$) increases and the relative permeability of the wetting fluid ($k_{\mathrm{w}}$) stays relatively constant as $M$ increases, as have several other experimental and numerical studies (Dou & Zhou, 2013; Goldsmith & Mason, 1963; Huang & Lu, 2009; Jeong et al., 2017; Mahmoudi et al., 2017; Yiotis et al., 2007; Zhao et al., 2017). An analytical study of co-current annular flow in which the wetting fluid is distributed on the pore surface and the nonwetting fluid is in the middle of the pore produced empirical equations for the nonwetting and wetting fluids as a function of $M$ and saturation:

$$k_{\mathrm{nw}} = S_{\mathrm{nw}} \left[\frac{3}{2} M + {S_{\mathrm{nw}}}^2 \left(1 - \frac{3}{2} M\right)\right] \qquad (3)$$

$$k_{\mathrm{w}} = \frac{1}{2}(1 - S_{\mathrm{w}})^2 (3 - S_{\mathrm{w}}) \qquad (4)$$

where $S_{\mathrm{nw}}$ is the saturation of the nonwetting fluid, and $S_{\mathrm{w}} = 1 - S_{\mathrm{nw}}$ is the saturation of the wetting fluid. These equations suggest that $k_{\mathrm{w}}$ is not affected by increasing $M$ and is a function of saturation alone. However, other studies have reported that $k_{\mathrm{nw}}$ increases and $k_{\mathrm{w}}$ decreases as $M$ increases (Ahmadlouydarab et al., 2012; Fan et al., 2019; Goel et al., 2016; Ramstad et al., 2010); thus, there is as yet no general agreement on the variation of $k_{\mathrm{w}}$ with increasing $M$. One of the challenges of previous studies was the difficulty of removing the effects of capillary forces and wettability factors when evaluating this relationship.

Similarly, studies of the influence of *Ca* on relative permeability is still incompletely known. In an experimental study, Fulcher et al. (1985) concluded that $k_{nw}$ is a function of IFT and viscosity variables individually rather than a function of the *Ca*, whereas $k_w$ can be modeled directly as a function of *Ca*. Several studies (Asar & Handy, 1989; Fan et al., 2019; Harbert, 1983) also found that both $k_{nw}$ and $k_w$ increase as IFT decreases because the two fluids interfere less with each other and thus tend to form more well-connected flow pathways. One of the studies (Asar & Handy, 1989) showed that both fluids relative permeability curves tend to straighten and approach the 45° tangent line as IFT approaches zero. Other studies (Amaefule & Handy, 1982; Fei Jiang et al., 2014; Shen et al., 2010) also concluded that both $k_{nw}$ and $k_w$ decrease as *Ca* decreases. On the other hand, a numerical study (Zhao et al., 2017) concluded that $k_w$ increases with increasing *Ca* under neutral wetting conditions ($\theta = 90°$) but stays relatively constant with increasing *Ca* under strong wetting conditions ($\theta = 135°$). These divergent results warrant further investigations of how relative permeability changes with changing IFT and *Ca*. One of the challenges in this evaluation is the difficulty of isolating the effect of IFT while keeping other parameters, such as viscosity, constant. In addition, *Ca* is a function of fluid velocity, which is a direct of from the simulation. Thus, it is difficult to hold *Ca* constant in all simulation conditions.

Previous studies have also demonstrated how the viscosity ratio can affect the breakup of fluid droplets. Instabilities due to the viscosity gradient at the interface of the two fluids cause fluid droplet deformation and breakup under viscous flow conditions when the Reynolds number is low (Bischofberger et al., 2015; Mu'min et al., 2021; Nekouei & Vanapalli, 2017; Stone, 1994). We suspect that the fluid droplet fragmentation mechanism is also one of the driving factors of the relative permeability change caused by the viscosity ratio. However, to the best of our knowledge, no research linking relative permeability variation to fluid droplet breakup caused by viscosity ratio variation has ever been done.

Previous studies have usually evaluated the separate effects of $M$ and $Ca$ on relative permeability. However, in two-phase flows, the effects of viscosity gradient and interfacial tension must be evaluated simultaneously to accurately predict the hydraulic properties in the system (Tsuji et al., 2016), including relative permeability. Because few studies have evaluated the condition when both parameters influence relative permeability using a steady-state simulation, our aim in this work was to fill that knowledge gap.

In this paper, we propose a method to simultaneously evaluate the effects of viscosity ratio $M$ and capillary number $Ca$ on relative permeability by creating a $M—Ca—k_{nw}$ relationship map (i.e., showing relative permeability on a diagram relating $M$ and $Ca$) by applying a color gradient Lattice Boltzmann method (LBM) simulation to a three-dimensional (3D) digital rock model. We begin by evaluating the effects of $M$ and $Ca$ individually on the relative permeabilities of the nonwetting and wetting fluids by holding other parameters constant. We also calculate the number of fluid clusters to describe the fluid connectedness, a factor that is directly related to relative permeability, and link the fluid connectedness to fluid droplet breakup. We then map $k_{\mathrm{nw}}$ for various $M$–$Ca$ conditions in search of general trends. We believe that such a map has never before been created, and that it will be useful for quickly estimating relative permeability if $M$ and $Ca$ are known. By understanding the variations of relative permeability in the $M$–$Ca$ parameter space, we can conduct accurate large-scale reservoir simulations by considering the reservoir conditions $M$ and $Ca$ and thereby contribute to the wide range of research regarding applications that employ two-phase fluid mixtures.

## 2 Methods

### 2.1 Lattice Boltzmann Method

The LBM is a branch of computational fluid dynamics that has emerged as a popular technique to solve multiphase fluid flow systems in complex geometries because of its algorithmic simplicity (S. Chen & Doolen, 1998; Dou & Zhou, 2013; Fei Jiang et al., 2014; Ramstad et al., 2010; Succi et al., 2010). LBM simulations treat fluids as a group consisting of fictive particles; the movement of these particles is simulated with a statistical approach. The movement of the bulk fluid is simulated from the propagation and collision processes of the fictive particles (Huang et al., 2011). We chose the Rothman–Keller color gradient model (Tölke et al., 2006) to conduct the simulations because it can simulate a high fluid viscosity ratio with better accuracy than other LBM models (Ahrenholz et al., 2008; Yang & Boek, 2013). The color gradient model is so named because it graphically represents two-phase fluids as a mixture of a wetting and nonwetting fluid, assigned the colors blue and red, respectively (Huang et al., 2015; Fei Jiang et al., 2022). Our 3D simulations used the D3Q19 (3 dimensions, 19 velocity lattice) velocity model.

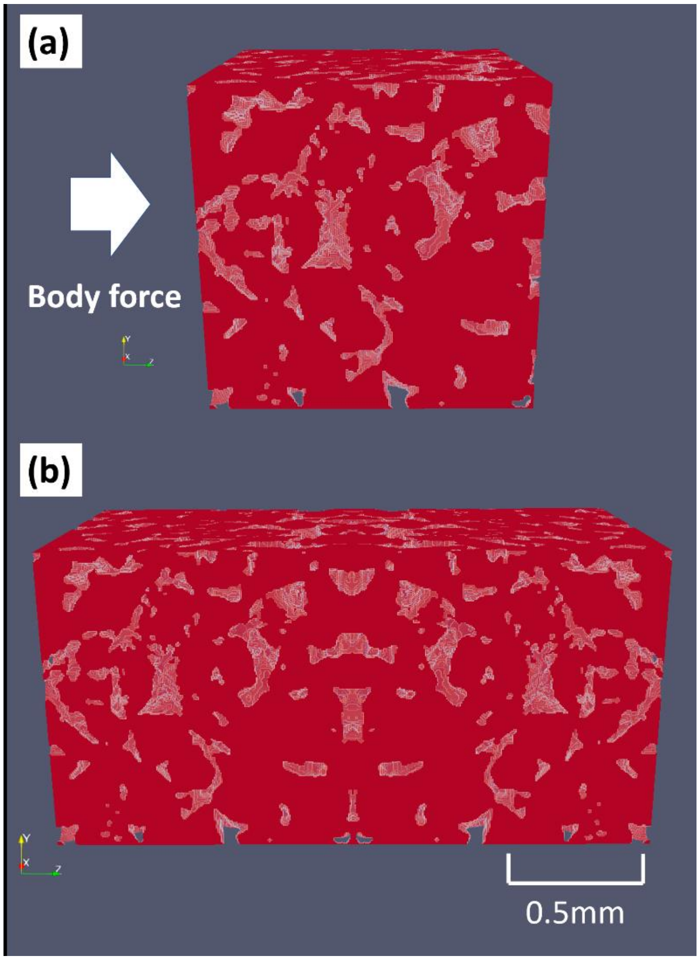


Fig. 1. Berea sandstone digital rock model: (a) core form and (b) mirrored form.

## 2.2 Digital rock model

We used a 3D digital rock model obtained from microtomographic images of Berea sandstone (Fig. 1a). Berea sandstone is chosen due to its relatively well-known properties (Øren & Bakke, 2003). The rock has a relatively large mean grain size of ∼250 μm and consists of quartz, feldspar, carbonates, and clay minerals. Its average pore size is ∼20 μm with an average throat size of ∼10 μm. Our rock model, obtained from the database of Dong and Blunt (2009), had an original resolution of 5.345 μm per pixel. To ensure that the digital rock resolution would be fine enough for the two-phase flow simulation conditions, each pixel was split into 2; hence, each pixel in our model represents 2.673 μm. The 3D digital rock is a stack of 400 tomographic images, and each image includes 400 × 400 pixels. Thus, the digital rock represents an actual size of 1.069 mm × 1.069 mm × 1.069 mm. The simulation requires a rock model that is larger than its representative elementary volume (~1 mm for Berea sandstone), and the multi-pore nature of the rock must be considered.

## 2.3 Relative permeability calculation

The viscosity ratio $M$ is defined by dividing the nonwetting fluid's viscosity ($\mu_{nw}$) by the wetting fluid's viscosity ($\mu_w$) (equation 1). In the LBM, $\mu$ can be calculated as follows:

$$\mu = \frac{1}{3}\left(\tau - \frac{1}{2}\right) \qquad (5)$$

where $\tau$ represents the relaxation parameter. Thus, the viscosities of both fluids can be modified by changing the $\tau$ value. Because $\tau$ must be larger than 0.5 for a positive viscosity and the simulation becomes unstable as $\tau$ approaches 0.5, it is important that the simulation uses a $\tau$ value that ensures its stability and accuracy. In this study, we altered $M$ only by changing the $\tau$ value of the nonwetting fluid to manipulate $\mu_{nw}$. The wetting fluid viscosity was kept constant at 0.1555 lu$^2$/ts (length$^2$/time in lattice units) in all simulations to preserve its stability. Changes in $M$ can be interpreted as a change in either $\mu_w$ or $\mu_{nw}$; thus, modifying either viscosity value will produce the same results if their ratio is maintained.

The capillary number $Ca$ can be modified based on equation (2) by changing the $\sigma$ and $\mu_{nw}$ parameters. Because $\mu_{nw}$ is also used to determine $M$, we achieved the desired $Ca$ by adjusting $\sigma$ alone. In the color gradient LBM model, $\sigma$ can be modeled by introducing a perturbation term into equilibrium equations based on the gradient of the phase field of the two fluids. Tölke et al. (2006) provides a detailed description of the model. The average velocity of the nonwetting fluid after the simulation had converged to equilibrium was used to calculate the *Ca* number. We adjusted $\sigma$ at every simulation point (every $M$ and in every saturation condition) to ensure that *Ca* had a similar value and fell within the permitted error range of log $Ca \pm 0.10$. When the fluid velocity change in the last 1,000 simulation steps was less than 2% for all cases, the simulations were assumed to have converged at that time. The time-averaged velocity value in the last 3,000 steps was calculated for further investigation.

To remove the complications arising from wettability effects, we assumed that the solid was completely nonwetting ($\theta = 180°$) to the nonwetting fluid in all conditions. Given that condition, the wetting fluid coats the surface of the rock, whereas the nonwetting fluid is not in contact with the pore wall and can only occupy the central parts of the pores.

We applied a steady-state simulation condition, which assumes that the wetting fluid saturation ($S_w$) and nonwetting fluid saturation ($S_{nw}$) are kept constant. In the initial state, both fluids were specified as being randomly distributed in the pore spaces. The initial condition was chosen because it allows each pore body to have roughly the same proportions of nonwetting and wetting fluid according to the prescribed saturation; thus, this condition produces an extremely uniform distribution of nonwetting and wetting fluid throughout the rock. In addition, because the initial fluid connectivity is reduced under this initial condition and increases capillary trapping, this initial distribution might be desirable in a CCS site (Fei Jiang & Tsuji, 2016). Under this initial condition, fluids are generated randomly in pore space; therefore, some nonwetting fluids touch the grain surface at the initial stage. As the simulation progresses, the wetting fluid coats the surface of the rock, and the nonwetting fluid moves to occupy only the central parts of pores because of the perfect wettability condition of the solid. A constant body force was applied in the $z$ direction to both fluids to mimic the pressure gradient: $g = dP/dz$ (Fig. 1a). For the interaction between rock solid nodes and fluid voxels, no-slip boundary conditions were applied by using the halfway bounce-back scheme (X. Li et al., 2016; Singh et al., 2017). The density of both fluids was set at 1.0 in lattice units, which corresponds to 1,000 kg/m$^3$ in the physical unit. We did this because our study was focused on viscosity differences, and the effect of density contrast is minor if inertial force can be neglected.

We applied a periodic boundary condition in the $x$, $y$, and $z$ directions of our 3D model. Specifically, in the flow direction ($z$ direction), the rock was mirrored to ensure that the pore spaces on the right side were connected to the left side of the digital rock (Fig. 1b) (F Jiang & Tsuji, 2017).

### 2.3.1 Relative permeability curve

The relative permeability curve is a plot of $k$ versus saturation $S_{nw}$. As $S_{nw}$ increases, $k_{nw}$ increases and $k_w$ decreases. The shape of this curve can change as a result of viscous drag force and capillary force; thus, an investigation of its variation with changes in $M$ and $Ca$ is important to determine the optimum conditions to achieve the desired value of $k$. We plotted $k_{nw}$ and $k_w$ as a function of $S_{nw}$ to create relative permeability curves for various conditions.

In this study, we plotted all permeability curves for $S_{nw}$ values within a wide range from 10% to 90%. Although some of these $S_{nw}$ values might be unrealistic in actual injection settings because of irreducible wetting phase saturation (Tsuji et al., 2016), we still considered those hypothetical $S_{nw}$ conditions for the ideal situation of a steady-state laboratory experiment.

### 2.3.2 $M$–$Ca$–$k_{nw}$ permeability color map

After confirming the influence of $M$ and $Ca$ on $k_{nw}$ and $k_w$ in a two-phase flow system, we conducted simulations at various $M$ and $Ca$ conditions with $S_{nw}$ held at a constant value of 20% to create a plot of $M$–$Ca$–$k_{nw}$ correlation or color diagram. The 20% $S_{nw}$ condition was chosen because it can realistically be achieved under all $M$–$Ca$ conditions (Tsuji et al., 2016). The color diagram is useful to evaluate the degree of influence of $M$ and $Ca$ on changes of relative permeability when both parameters influence a system, and can also provide estimates of relative permeability in a reservoir under a wide range of $M$ and $Ca$.

## 3 Results and interpretation

Before conducting simulations in various $M$ and $Ca$ conditions, we first ran single-phase simulations to determine the absolute permeability value of the porous media and to verify the stability of the simulation. The results are presented in Appendix A. Afterwards, the effects of $M$ and $Ca$ were then evaluated individually to see how they influence nonwetting and wetting relative permeability curves in a two-phase flow system. Next, we conducted simulations over a wide range of $M$ and $Ca$ values at a $S_{nw}$ value of 20% to create a relative permeability color diagram.

### 3.1 Relative permeability curve from a two-phase simulation

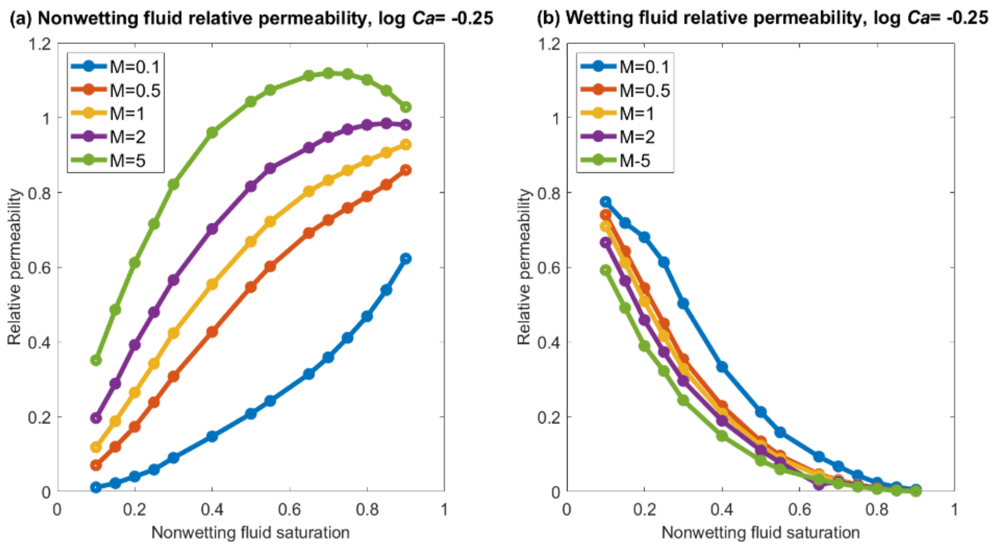


Fig. 2. Relative permeability curves as a function of *M* at constant log *Ca* = −0.25 ± 0.1 for *M* = 0.1–5: (a) nonwetting fluid relative permeability ($k_{nw}$) curve and (b) wetting fluid relative permeability ($k_w$) curve.

### 3.1.1 Effect of changes in *M* on $k_{nw}$ and $k_w$

We plotted values of $k_{nw}$ for five values of *M* (0.1, 0.5, 1, 2, and 5) over the range of $S_{nw}$ (10% to 90%) while holding log *Ca* nearly constant at −0.25 ± 0.10 (Fig. 2a). We evaluated the two-phase flow at high *Ca* to completely remove the capillary force effect. In all simulation conditions, the Reynolds number must not exceed 10 (Bear, 1975). The maximum Reynolds number reached in this set of simulations was 5.27 and 9.50 for nonwetting and wetting fluid, respectively. The *M* values (0.1, 0.5, 1, 2, and 5) were chosen to represent a wide range of mobility conditions, from an extremely unfavorable to an extremely favorable mobility condition. The $k_{nw}$ value increased as *M* increased, especially for intermediate $S_{nw}$ values (30% to 70%). For *M* = 5, $k_{nw}$ exceeded 1 under some $S_{nw}$ conditions; that is, it exceeded the intrinsic permeability of the rock. This result agrees with previous studies and can be explained by the lubrication effect, also known as the viscous coupling effect (Goel et al., 2016; Fei Jiang et al., 2021; H. Li et al., 2005; Ramstad et al., 2010; Yiotis et al., 2007; Zhao et al., 2017).

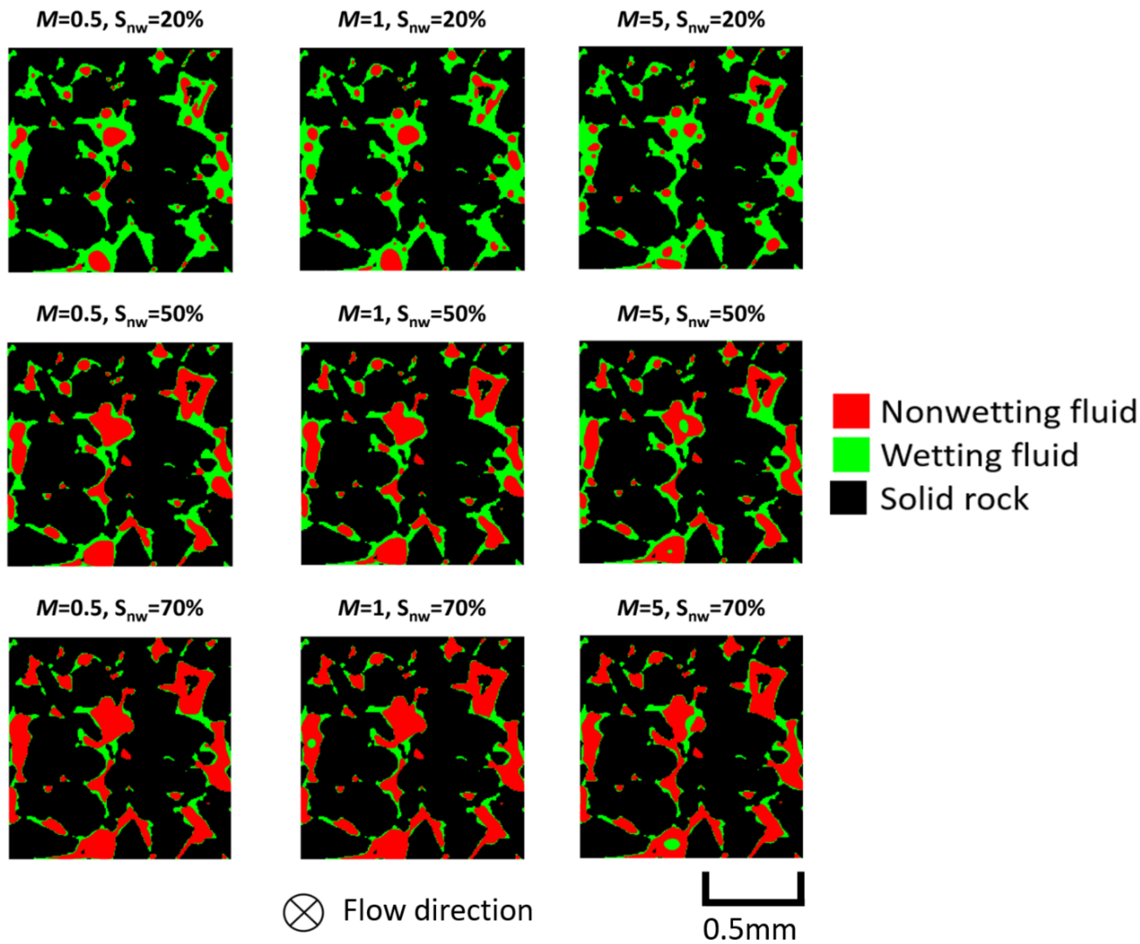


Fig. 3. Two-dimensional slice showing the distributions of nonwetting fluid (red), wetting fluid (green), and solid rock (black) at various values of $M$ and $S_{nw}$.

To illustrate the lubrication effect, we provide a 2D image showing the distribution of nonwetting fluid, wetting fluid, and solid rock at the final state of the simulation under various $M$ and $S_{nw}$ conditions (Fig. 3). Because the wetting fluid (green) layer is generally present between the nonwetting fluid and the rock, the wetting fluid moves along the rock surface and the nonwetting phase is confined to the central part of the pore. Thus, the velocity of the nonwetting fluid is affected only by the momentum transfer across fluid–fluid interfaces and not by contact with the grain surface.

At sufficiently high values of $M$, the wetting fluid acts as a lubricant that enhances the movement of the nonwetting fluid, making its permeability higher than in the single-phase condition such that $k_{\mathrm{nw}}$ is greater than 1 (Fig. 2a). This lubrication effect most strongly affects $k_{\mathrm{nw}}$ in the intermediate $S_{\mathrm{nw}}$ range, when the wetting fluid forms thick films that provide the nonwetting fluid with a moving boundary (Vafai, 2000). At low $S_{\mathrm{nw}}$, the nonwetting phase tends to form droplets with low connectivity; thus, the lubrication effect is less pronounced. At high $S_{\mathrm{nw}}$, $k_{\mathrm{nw}}$ also decreases toward unity because less wetting fluid is present in the rock and the nonwetting phase comes into contact with the rock, degrading the lubrication effect and reducing $k_{\mathrm{nw}}$ near to the single-phase condition. Because the lubrication effect occurs at high $M$ values, it is commonly observed in mixtures of heavy oil and water in EOR systems and has been confirmed by experimental results (Goel et al., 2016; Shad et al., 2008).

In addition to the lubrication effect, the relative permeability change due to the viscosity ratio can be linked to local pore-filling behavior. Because of the body force, a nonwetting fluid droplet can move from one pore body to neighboring pore bodies. As $M$ increases, as a result of favorable mobility conditions, there is more chance for nonwetting fluid droplets to move to several neighboring pore bodies through the narrow pore throats (Bakhshian et al., 2021), causing fluid droplet fragmentation and thereby enabling the fluid to occupy smaller pore spaces. This might be one of the contributing factors causing $k_{\mathrm{nw}}$ to exceed 1 when $M = 5$ at intermediate saturation. Furthermore, under high $S_{\mathrm{nw}}$, nonwetting fluid already exists in most of the pore bodies throughout the simulation time; thus, locally occurring pore-filling behavior effects decrease, causing $k_{\mathrm{nw}}$ to decrease towards unity under high $S_{\mathrm{nw}}$ conditions.

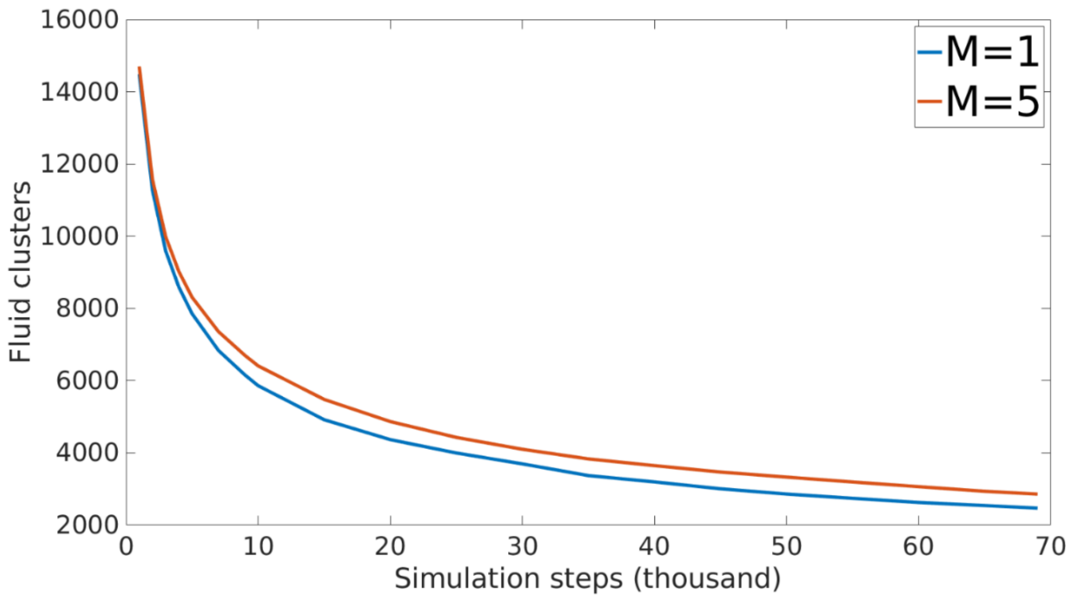


Fig. 4. Evolution of the number of clusters of nonwetting fluid at $M$ = 1 and $M$ = 5, with $S_{nw}$ = 20% and log $Ca$ = −0.25 ± 0.1.

To investigate nonwetting fluid droplet fragmentation throughout the simulation, we considered the evolution of the number of nonwetting fluid clusters during simulations with $M$ = 1 and $M$ = 5, log $Ca$ = −0.25 ± 0.10, and $S_{nw}$ = 20% (Fig. 4). Throughout the simulations, the number of nonwetting clusters for both simulation conditions decreases, suggesting that some of the nonwetting fluid clusters become more connected and form larger clusters as the simulation proceeds. In the final converged condition, the number of nonwetting fluid clusters is higher for $M$ = 5 than for $M$ = 1. This result indicates that the nonwetting fluid at $M$ = 5 forms more individual clusters and has less fluid connectivity than at $M$ = 1. This difference is the result of the instability of the interface of the fluids due to the viscosity stratification (Yiantsios & Higgins, 1988; Yih, 1967). When two immiscible fluids have different viscosities, their velocities will also be different at their interface, causing instability. The instability causes the nonwetting fluid to create more clusters. This result agrees with past research and our hypothesis that instability at the fluid interface can cause fluid droplet fragmentation (Bischofberger et al., 2015; Mu'min et al., 2021; Nekouei & Vanapalli, 2017; Stone, 1994). As more fluid clusters are formed, the size of the nonwetting fluid clusters is smaller, and it is easier for them to pass through the pore space. At $M = 1$, the nonwetting fluid is more connected and its fluid clusters are larger. The larger clusters cannot pass through the small pore throats, leading to lower $k_{nw}$.

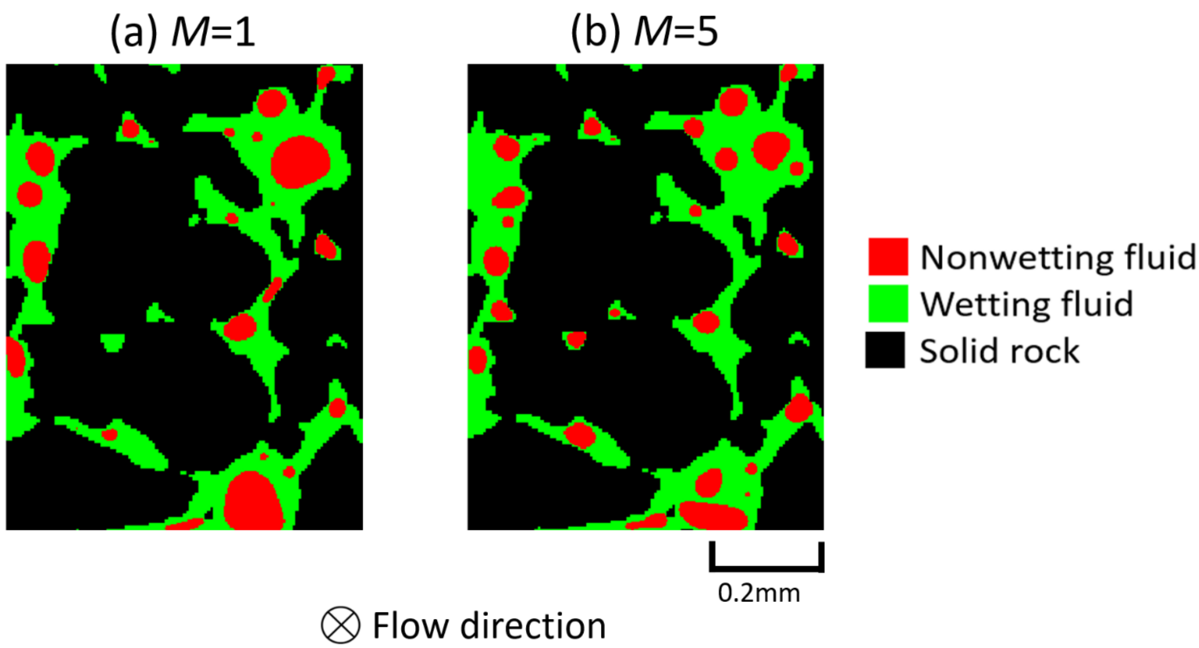


Fig. 5. Two-dimensional slice showing the distributions of nonwetting (red), wetting fluid (green), and solid rock (black) at (a) $M = 1$ and (b) $M = 5$ at 20% $S_{nw}$. These images show a portion of the slice illustrated in Fig. 3.

To obtain further insights into fluid cluster size, we provide an illustration showing nonwetting and wetting fluid distributions in an enlarged section of a 2D slice of the simulated specimen for $M = 1$ and $M = 5$ at log $Ca = -0.25 \pm 0.10$ and 20% saturation after the simulation had converged (Fig. 5). The nonwetting fluid (red) at $M = 1$ forms larger clusters in the pore throat, whereas at $M = 5$, the nonwetting fluid forms a larger number of clusters but the size of each cluster is smaller. This result is comparable to our findings (shown in Fig. 4) that nonwetting fluid droplet fragmentation occurs as a result of instability at the fluid interface as $M$ increases. Because the nonwetting fluid clusters are smaller, it is easier for them to pass through the pore space, leading to higher $k_{nw}$. Furthermore, the wetting fluid (green) coats the grain surface under both conditions and produces a lubrication effect (Fig. 5).

Our results also demonstrate that $k_w$ decreases as $M$ increases (Fig. 2b), mainly when nonwetting fluid saturation is low. This phenomenon can be attributed to an increase of shear force from the nonwetting phase. As $M$ increases and nonwetting fluid droplet fragmentation occurs, the wetting fluid has a larger contact area with the nonwetting fluid (Fig. 5). As a result, the wetting fluid receives a higher shear force from the nonwetting fluid, which inhibits the flow of the wetting fluid so that it has a lower velocity. In addition, as wetting fluid saturation decreases, the $k_w$ gaps under all $M$ conditions become smaller.

To confirm our interpretation, we calculated the degree of contact between nonwetting and wetting fluid by calculating the number of wetting fluid voxels that were adjacent to a nonwetting fluid voxel, for conditions of $M$ = 1 and $M$ = 5 at log $Ca$ = −0.25 ± 0.10 and $S_{nw}$= 20%. When the simulations converged, 13.77679% and 13.88825% of wetting fluid voxels were adjacent to nonwetting fluid voxels at $M$ = 1 and $M$ = 5, respectively. This result shows that, at $M$ = 5, the wetting phase fluid has a higher degree of contact with the nonwetting fluid and receives more drag force from the nonwetting fluid; thus, $k_w$ is lower at $M$ = 5 than at $M$ = 1, as shown in Fig. 2b.

In addition, Zhao et al. (2017) suggested that the $k_w$ decrease in response to an $M$ increase occurs because the wetting fluid is more attached to the grain surface when the viscosity ratio is large. When the viscosity ratio is high, fragmentation of the nonwetting phase tends to occur easily and the fragments move towards the centers of pore bodies, so that wetting fluid can easily move to coat the grain surface. Consequently, because the wetting fluid has a larger contact area with the grain surface, it receives more shear drag force, which causes a decrease in velocity. To confirm our interpretation, we calculated the degree of contact between the wetting fluid and the grain surface, as indicated by the number of wetting fluid voxels having a solid surface as a neighbor, for $M = 1$ and $M = 5$ at $\log Ca = -0.25 \pm 0.10$ and $S_{nw} = 20\%-70\%$ after the simulation had converged (Table 1).

| | **$M$=1** | **$M$=5** |
|---|---|---|
| **$S_{nw}$=20%** | 36.79546% | 36.74534% |
| **$S_{nw}$=50%** | 50.94340% | 51.18913% |
| **$S_{nw}$=70%** | 67.81628% | 68.25865% |

Table 1. Percentage of wetting fluid that has a grain surface as a neighbor voxel fluid at $M = 1$ and $M = 5$, with $S_{nw}$ of 20%−70% and $\log Ca = -0.25 \pm 0.1$, after the simulation has converged.

At $S_{nw} = 20\%$, the percentage of wetting fluid voxels adjacent to a solid surface is low, because the wetting fluid film between the nonwetting fluid and grain surface is thick (Fig. 3) and only a small portion of the wetting fluid is in direct contact with the grain surface. The values for $M = 1$ and $M = 5$ are also similar, suggesting that the nonwetting fluid at low $S_{nw}$ has less chance to approach the rock surface because of the thick wetting fluid film even as $M$ increases. Thus, at low $S_{nw}$, the dominant cause of the $k_w$ decrease is the shear force at the fluid interface and not the shear drag force at the wall. When $S_{nw} = 50\%$ and 70% and $M = 5$, the proportion of the wetting phase fluid attached to the grain surface increases compared to when $M = 1$, indicating that the wetting fluid has a higher degree of contact and receives more drag force from the solid wall. Thus, $k_w$ at $M = 5$ is lower than that at $M = 1$ (Fig. 2b).

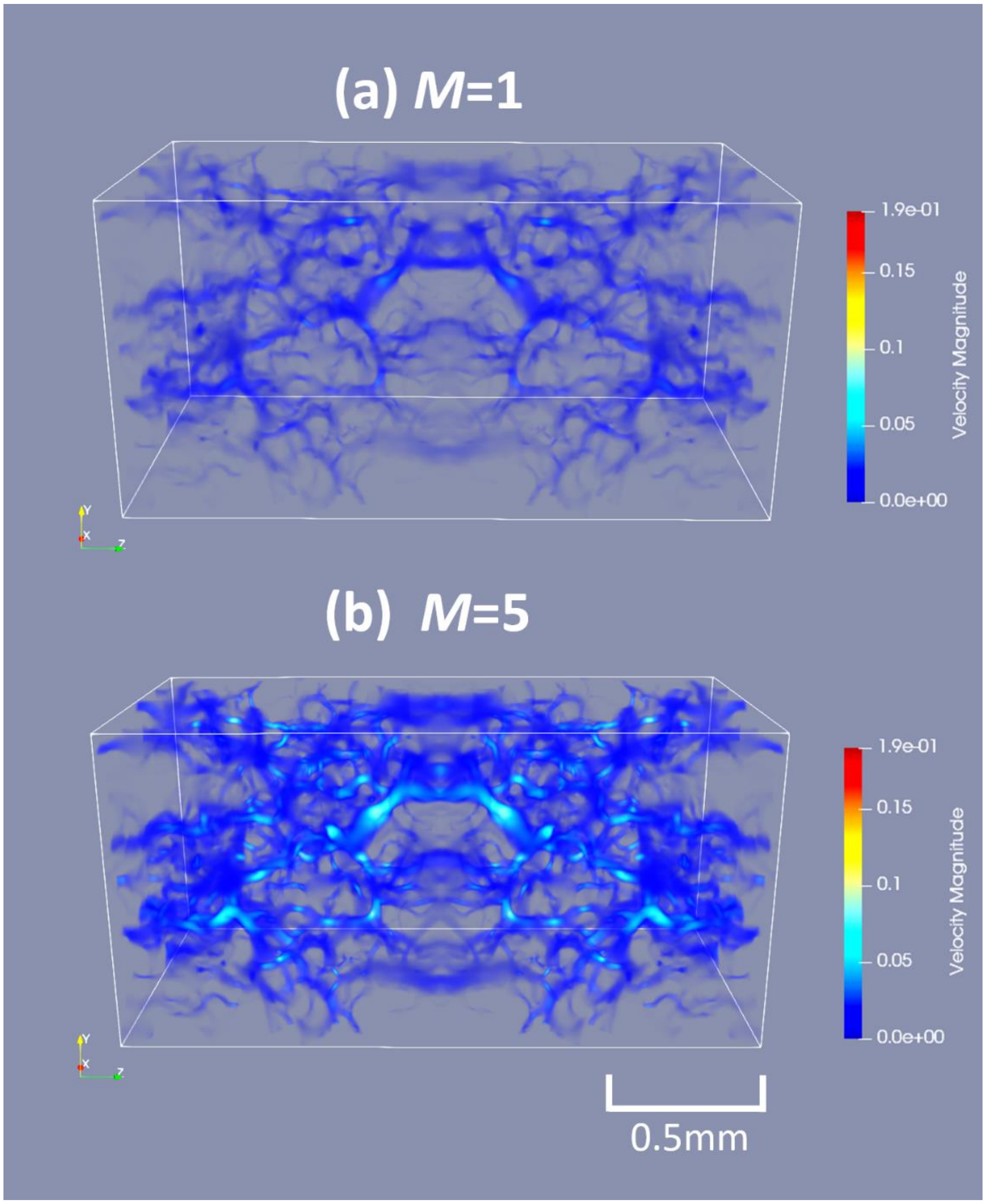


Fig. 6. Normalized velocity fields for the nonwetting fluid in a two-phase simulation with (a) $M$ = 1 and (b) $M$ = 5, at log $Ca$ = −0.25 ± 0.1 and $S_{nw}$ = 20%.

The results of fluid velocity for $M$=1 and $M$=5 in the pore spaces at 20% saturation after the simulation converges are plotted in Figs. 6a and 6b, respectively. The fluid velocity field in Fig. 6 is normalized to consider the effect of viscosity change using the equation $U^* = \frac{U}{\Delta PL/\mu}$. It can be seen that the normalized fluid velocity is higher at $M$ = 5 than at $M$ = 1, indicating that $k_{nw}$ is higher at $M$ = 5 than at $M$ = 1, in agreement with our relative permeability curve.

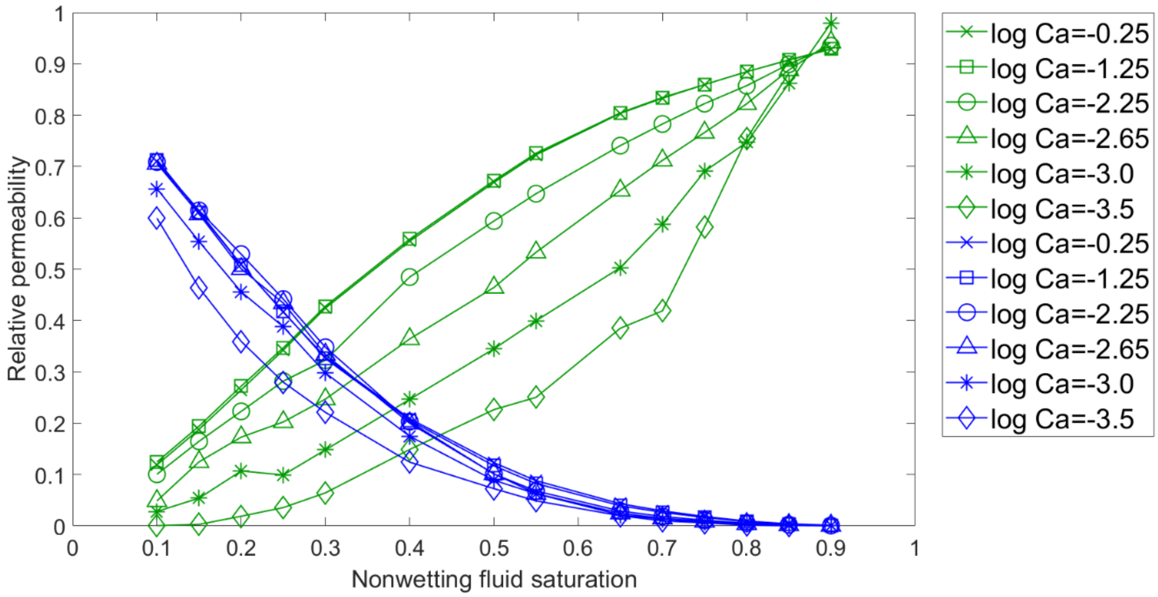


Fig. 7. Relative permeability curves for the nonwetting ($k_{nw}$, green) and wetting fluids ($k_w$, blue) for log *Ca* = −0.25 to −3.5 with *M* = 1.

3.1.2 Effect of *Ca* change on $k_{nw}$ and $k_w$

The $k_{nw}$ and $k_w$ curves for six different values of log *Ca* (−0.25, −1.25, −2.25, −2.65, -3.00, and -3.50 ± 0.10) at *M* = 1 are plotted (Fig. 7). The *Ca* value is altered by changing the IFT value. It was difficult to keep *Ca* constant because *Ca* is also a function of fluid velocity, which is a direct result of the simulation. Thus, we allowed a small error of ± 0.10 for *Ca* under all conditions.

The $k_{nw}$ values remain relatively constant between log *Ca* = −0.25 and −1.25, i.e., for high *Ca*/low IFT values, and the relative permeability curve for the nonwetting fluid is an approximately straight line, in agreement with previous studies (Asar & Handy, 1989; Shen et al., 2010). However, as log $Ca$ becomes lower than −1.25, $k_{nw}$ notably decreases as $Ca$ decreases. This decrease occurs because the flow of the nonwetting fluid is more strongly inhibited by capillary force when $Ca$ is low. Capillary force is controlled by IFT, the surface tension forces between the nonwetting and wetting fluids. As IFT increases, the nonwetting fluid becomes trapped by the larger capillary force in the small pore spaces, thus causing $k_{nw}$ to decrease. This result also suggests that $k_{nw}$ does not decrease linearly with changes in IFT/$Ca$, because the $k_{nw}$ decrease gap gradually becomes larger as $Ca$ decreases. This phenomenon occurs because as $Ca$ becomes lower, the influence of capillary force becomes more dominant.

For the wetting fluid, $k_w$ also decreases as $Ca$ decreases (Fig. 7), but at a much smaller rate compared to $k_{nw}$, consistent with previous research (Harbert, 1983; Fei Jiang et al., 2014; McDougall et al., 2007; Ramstad et al., 2010; Zhao et al., 2017). The reason for this result is that the wetting fluid flows only along the rock surface and the nonwetting fluid flows in the central part of the pores (Fig. 3). Thus, the wetting fluid is mainly affected by interaction with the rock surface, and the change in capillary force has a negligible effect. However, when $Ca$ is low (log $Ca$ = −3.50), the $k_w$ decrease is more notable. This phenomenon can be attributed to the drag force exerted by the nonwetting fluid. At log $Ca$ = −3.50, $k_{nw}$ becomes notably lower compared to other $Ca$ conditions and the nonwetting fluid velocity is low. This result suggests that the influence of the nonwetting fluid drag force on the wetting fluid increases, causing $k_w$ to markedly decrease with the $k_{nw}$ decrease. Nevertheless, we conclude that the variation in $k_w$ is dominated by the fluid saturation in the system and is little affected by changes in IFT or $Ca$.

### 3.2 $M$–$Ca$–$k_{nw}$ color diagram

After confirming the influence of $M$ and $Ca$ on $k_{nw}$ and $k_w$ in a two-phase flow system, we conducted simulations with various values of $M$ and $Ca$ at a constant 20% $S_{nw}$ to create a $M$–$Ca$–$k_{nw}$ correlation diagram (Fig. 8). We chose the 20% $S_{nw}$ condition because it is realistic under all $M$–$Ca$ conditions (Tsuji et al., 2016). We created the color diagram only for the nonwetting fluid because the relative permeability curves (Fig. 7) demonstrate that $k_w$ does not respond markedly to changes in $Ca$. We also created a regression model and equation for our results reported in this section (see Appendix B). The maximum Reynolds number reached in this set of simulations was 3.92 for $M = 0.10$ and $\log Ca \approx 0$.

Color maps are useful to provide estimates of $k_{nw}$ under a wide range of $M$ and $Ca$ conditions in a reservoir and to analyze the degree of influence on $k_{nw}$ by $M$ and $Ca$ (Fig. 8). The first color map (Fig. 8a) depicts the parameter space of $\log M = -1.02$ to 0.70 and $\log Ca = -4.00$ to 0.00, which represents the broad range of conditions that can be simulated. Values higher than this range are hard to achieve at the field scale, and lower values are outside the stable range of the simulation. The second color map (Fig. 8b), covering the lower left quadrant of the parameter range shown in Fig. 8a with parameter space of $\log M = -1.02$ to 0.00 and $\log Ca = -4.00$ to -1.00, was produced to increase the accuracy of $k_{nw}$ estimates for a system with low $M$ and low $Ca$, which is common in CCS field.

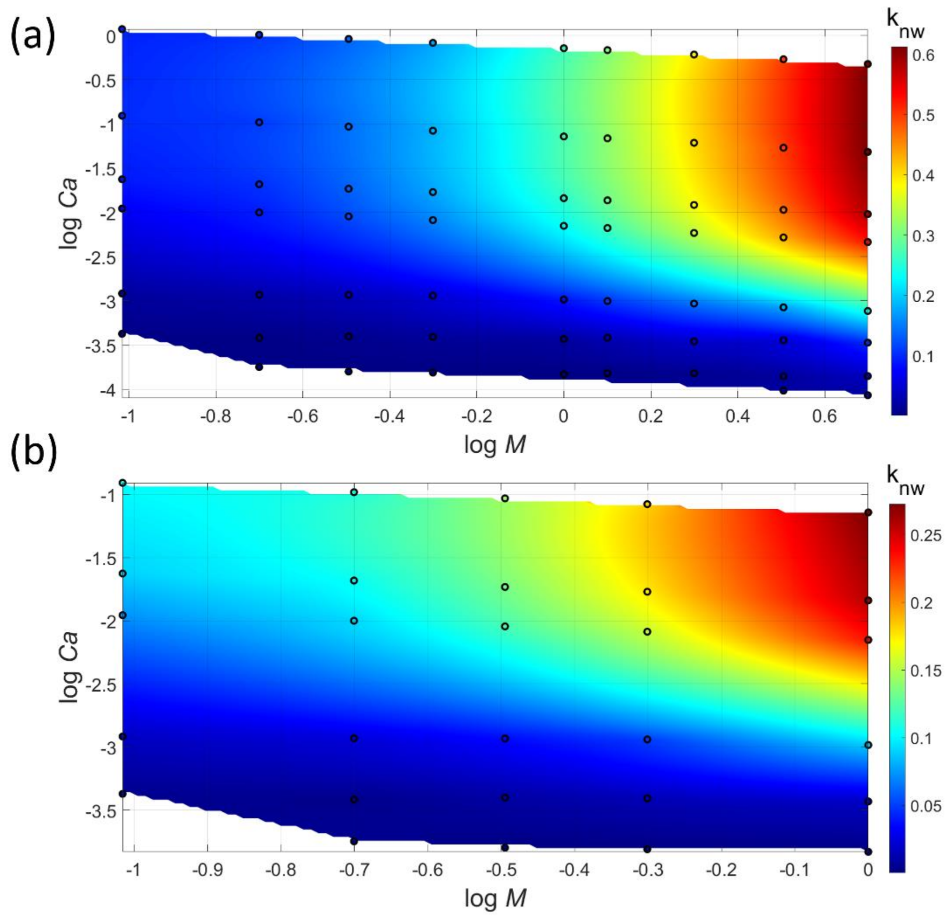


Fig. 8. Relative permeability map of the nonwetting fluid for (a) log *M* = −1.02 to 0.70 and log *Ca* = −4.00 to 0.00, and (b) log *M* = −1.02 to 0.00 and log *Ca* = −4.00 to −1.00. The dots indicate the *Ca*–*M* conditions used for LBM simulation.

In the specified parameter range, $k_{\mathrm{nw}}$ varies from 0.0002 to 0.6125 (Fig. 8a). For high log *Ca* values (between −1.25 to 0.00), $k_{\mathrm{nw}}$ does not vary with log *Ca* and is only influenced by *M*, as indicated by the almost straight vertical borders between color bands. This finding agrees with our results from section 3.1.2 (Fig. 7), which shows that for log $Ca \geq -1.25$, the nonwetting fluid relative permeability curve is not affected by *Ca*. However, as log *Ca* becomes lower than −1.25 (*Ca* value ≈ 0.06), $k_{\mathrm{nw}}$ can be seen to vary on both the *x* axis (log *M*) and the *y* axis (log *Ca*), that is, $k_{\mathrm{nw}}$ starts to be affected by the capillary force. The diagram agrees with our finding in section 3.2 that for log *Ca* lower than −1.25, $k_{\mathrm{nw}}$ decreases as *Ca* decreases.

The $k_{nw}$ variation with $M$ ($x$ axis) is more pronounced for log $M > 0$ ($M > 1$) than for log $M < 0$ (Fig. 8a). This result is consistent with our findings in section 3.1 and is caused by the lubrication effect resulting from viscosity differences. When $\mu_{nw}$ is higher than $\mu_w$, the resulting instability and viscous coupling effect enhance the relative permeability of the nonwetting fluid. The diagram clearly captures the contrast between $k_{nw}$ at log $M < 0$ and at log $M > 0$.

To check the detailed $k_{nw}$ variation under low $M$ and low $Ca$ conditions, in Fig. 8b we show an enlargement of part of the lower left quadrant of the parameter range illustrated in Fig. 8a. The $k_{nw}$ value range is 0.0002 to 0.2725 in Fig. 8b, and in this parameter space, both $Ca$ and $M$ influence $k_{nw}$ and thus the borders between the color bands are curved. In a CCS field, $M$ is usually lower than 1 and $Ca$ is generally low (Zheng et al., 2017). Therefore, Fig. 8b is useful for estimating nonwetting fluid relative permeability in a CCS field.

The diagram is useful for evaluating $k_{nw}$ when the effects of $M$ and $Ca$ are considered simultaneously, and the graph neatly summarizes all the main results of this study. The diagram shows that capillary force starts affecting the flow of the nonwetting fluid when log $Ca$ is less than −1.25 and that the effect of changes in $Ca$ may be just as important as that of changes in $M$. The graph also shows that $k_{nw}$ is affected by $M$ under all conditions, but most markedly when log $M > 0$. The graph yields a good estimate of $k_{nw}$ at 20% saturation based on the $M$ and $Ca$ parameters.

## 4 Discussion

We have demonstrated how $M$ and $Ca$ can markedly change the relative permeabilities of the nonwetting and wetting fluids in a reservoir; thus, our results can help identify the optimum properties of the immiscible fluids to be used in a geologic reservoir. For example, in a CCS project, the injectivity of the $CO_2$ is highest when the reservoir fluid has a lower viscosity and the IFT between the two fluids is low. Thus, the relative permeability of injected $CO_2$ is higher in a saline aquifer than in an oil field. For an EOR project, the relative permeability of oil is higher when a fluid with low viscosity is injected.

The relative permeability map (Fig. 8) is useful to provide accurate estimates of $k_{nw}$ in reservoir-scale simulations. Currently, the relative permeabilities of the nonwetting and wetting fluid are simulated on the basis of a uniform relative permeability curve, without regard to the *M* and *Ca* conditions. However, we have shown that the nonwetting fluid, at a typical saturation ($S_{nw}$) of 20%, can vary in relative permeability by an order of magnitude, from 0.0002 to 0.6125, depending on *M* and *Ca* conditions. The color map created in this study can provide more accurate estimates of relative permeability (e.g., temporal permeability variations in a 3D reservoir model) if *Ca* and *M* are derived from the reservoir simulation. In addition, although the *M* generally remains constant in the two-phase flow, the *Ca* value can greatly changes depending on the distance from the injection well in a reservoir. For example, when evaluating the reservoir area located near the injection well, the injection pressure creates a high-pressure gradient which causes the injected fluid velocity to be high. As the fluid flows away from the injection site, the fluid velocity becomes slower, thus the *Ca* becomes lower. This means that fluid relative permeability varies based on location inside the reservoir, and the permeability variation can be evaluated using the relative permeability map, thus providing a more accurate relative permeability estimation.

In this study, we conducted the simulation under steady-state conditions, as being most representative for illustrating fluid flows in a reservoir area distant from the injection site, where boundary effects are negligible (Honarpour et al., 2018; Ramstad et al., 2012). In addition, under steady-state conditions, relative permeability can be measured directly by using Darcy's law; thus, the relative permeability value is more accurate than one calculated under non-steady-state conditions. However, there are some differences between relative permeability values obtained under steady-state and non-steady-state conditions, and there are also some limitations to steady-state simulations. Under steady-state conditions, both fluid phases coexist together in the reservoir at the prescribed saturation from the beginning of the simulation. In contrast, under non-steady-state conditions, the reservoir is initially filled with wetting fluid, and nonwetting fluid is injected and gradually displaces the wetting fluid, which results in a gradual increase of nonwetting fluid saturation and a decrease of wetting fluid saturation. As a result, under non-steady-state conditions several factors can affect relative permeability variation, such as fingering phenomena, drainage and imbibition conditions, and the pore-filling behavior during the injection (Bakhshian et al., 2021; Rabbani et al., 2017). Therefore, an unsteady-state simulation can better represent relative permeability near the borehole or injection site, where remarkable displacement occurs. Nevertheless, if considering the law of two-phase fluid flow that coexist and flow together throughout the whole drainage area, steady-state relative permeability curves are more suitable for planning the whole reservoir design. In addition, relative permeability obtained under steady-state conditions is more accurate because the relative permeability can be directly measured by using Darcy's law. In contrast, in an unsteady-state simulation, relative permeability must be calculated from the capillary pressure change and production data under several assumptions (e.g., the Johnson, Bossler, and Naumann method; (Esmaeili et al., 2020; Johnson et al., 1959)). As a result, the obtained relative permeability is less accurate. Steady-state condition is also better to estimate relative permeability for CCS monitoring system after injection, as at the time, the $CO_2$ will coexist with the wetting fluid in the reservoir.

In this study, we created a relative permeability map for $S_{nw}$ = 20%, which is a reasonable condition that can be achieved in all or most systems. As $S_{nw}$ increases, $k_{nw}$ also increases until it reaches its maximum value (e.g., $k_{nw}$ at the irreducible saturation). Therefore, it is advisable to create relative permeability maps for several saturation conditions. One possible future direction from this study would be to create a four-dimensional $M$–$Ca$–$S_{nw}$–$k_{nw}$ graph to yield $k_{nw}$ estimates for all saturation conditions. Nevertheless, the great consistency of variations in $k$ caused by changes in $M$ and $Ca$ found in this study suggests that maps for other saturation conditions will have similar features to Fig. 8. It would also be possible to create a regression model for $k_{nw} = f(M–Ca–S_{nw})$ to estimate $k_{nw}$ under all saturation conditions.

In this study, we produced a relative permeability diagram for a digital specimen of Berea sandstone. In addition to $M$ and $Ca$, the influences upon relative permeability include the pore geometry of the rock, such as pore size distribution, pore connectivity, and other parameters (Jiang et al. 2018, WRR). These parameters differ among rock formations, meaning that the relative permeability maps of different types of reservoir rocks will vary. Our methodology makes it possible to create accurate maps of relative permeability for other reservoir rocks.

In this study, we used log $M$ ranging from −1.02 to 0.70 and log $Ca$ ranging from −4.00 to 0.00; however, in the $CO_2$ injection process, log $M$ might reach as low as −1.8 and log $Ca$ might reach −6.8 (Zheng et al., 2017). Such values are outside the stable range where this simulation can be applied. Nevertheless, the objective of this study was just to propose a method to predict the relative permeability of a two-phase flow fluid in a reservoir by using a color map diagram to evaluate the effect of the viscosity ratio and capillary number (Fig. 8). In a future study, we plan to improve the stability range of the simulation to allow lower $M$ and $Ca$ values to be considered.

In geological $CO_2$ storage, the maximum amount of $CO_2$ that can be stored and the injectivity of the $CO_2$ into the reservoir must both be considered (Tsuji et al., 2016). Thus, the results of this study must be combined with information on the effects of $M$ and $Ca$ on the maximum saturation of the nonwetting fluid. In this study, we showed that, for $CO_2$ as the nonwetting fluid, the relative permeability increases as $M$ increases and decreases as $Ca$ becomes very small. In contrast, Tsuji et al. (2016) demonstrated that the maximum $S_{nw}$ increases as $M$ increases and notably increases at low $Ca$. Thus, although a high value of $M$ is desirable to increase both the $CO_2$ capacity and injectivity, a low $Ca$ value can also increase the maximum $CO_2$ saturation but at the cost of reduced relative permeability. Both factors must be taken into account when choosing suitable conditions for $CO_2$ storage.

An advantage of using $M$ and $Ca$ is that both parameters are dimensionless, meaning that the results obtained in this pore-scale study can potentially be upscaled to the reservoir scale. Ideally, the pore-scale results are also valid at the reservoir scale as long as the ratios of the parameters (viscosity and IFT) are maintained for both fluids, because the fluid flow behavior at the reservoir scale is controlled by the fluid dynamics at the pore scale. However, this ideal is challenged by the inhomogeneity of the porous medium. The relative permeability is likely to vary throughout the reservoir due to differences in pore size, pore connectivity, and many other factors. Nevertheless, the results of a pore-scale simulation are important to verify relative permeability variations arising from selected factors (in this study, $M$ and $Ca$) by eliminating other factors. The results of a pore-scale study of relative permeability could then be upscaled by considering the structural factors of the reservoir, e.g., its porosity and pore connectivity, using advanced techniques such as machine learning.

## 5 Summary

To evaluate the influence of viscosity ratio $M$ and capillary number $Ca$ on relative permeability $k$ in a two-phase flow system, we calculated $k$ for nonwetting and wetting fluids ($k_{nw}$ and $k_w$) under various $M$ and $Ca$ conditions using an LBM simulation. The main results of this study are as follows.

1) In our simulations, the relative permeability of the nonwetting fluid increased as the viscosity ratio increased due to the lubricating effect, locally occurred pore-filling behavior, and instability of the fluid interface. Specifically, at high viscosity ratios ($M$ = 5), $k_{nw}$ could exceed 1 as a result of the lubricating effect.
2) The relative permeability of the wetting fluid decreased as $M$ increased due to the increase in shear force from the nonwetting fluid (viscous coupling effect)
3) As $M$ increased, the number nonwetting fluid clusters became higher, indicating that the nonwetting fluid became more disconnected and the size of each clusters becomes smaller.
4) At high capillary numbers (log $Ca$ = -0.25 to −1.25), $k_{nw}$ did not respond to $Ca$, however as log $Ca$ becomes lower than −1.25, $k_{nw}$ decreases as $Ca$ decreases due to the capillary force effect.
5) As $Ca$ decreased $k_w$ decreased, but at a negligible rate compared to $k_{nw}$.

6) $k_{nw}$ can change markedly in a wide range of *M*–*Ca* parameter space, and the *M*–*Ca*–$k_{nw}$ correlation map created in this study can provide $k_{nw}$ estimates at various reservoir conditions.

**Acknowledgements**

This study was supported by the Japan Society for the Promotion of Science (JSPS) through a Grant-in-Aid for Challenging Exploratory Research (Grant Number JP20K20948). This work was also partially supported by the JSPS KAKENHI Grant Number JP19K15100. We are grateful for the funding provided by the Top Global University project conducted by the Ministry of Education, Culture, Sports, and Technology, Japan (MEXT). We also gratefully acknowledge support of International Institute for Carbon-Neutral Energy Research ($I^2$CNER). The Micro-CT data used to reconstruct the digital rock model is achieved by The Imperial College Consortium on Pore-Scale Modelling and Imaging.

**Appendices**

A. Single-phase simulation

Before conducting the two-phase flow simulations, we first ran single-phase simulations to calculate the absolute permeability of the 3D rock model. Single-phase simulations can also be used to verify the accuracy and precision of the simulation. When only one type of fluid exists in a rock, the absolute permeability can be calculated from Darcy's law:

$$k = \frac{v\,\mu\,\Delta l}{\Delta P} \qquad \text{(A.1)}$$

where $k$ is the absolute permeability ($m^2$), $v$ is the average fluid velocity (m/s), $\mu$ is the dynamic viscosity of the fluid (Pa s), $\Delta l$ is the distance between the inlet and the outlet, and $\Delta P$ is the applied pressure difference between the inlet and the outlet. In this study, because the body force was applied only in the *z* direction, we calculated *k* in the *z* direction ($k_z$).

Because all simulation units are in lattice Boltzmann units, they must subsequently be converted into physical units. The unit conversion for *k* can be performed using the formula:

$$k_{(physical)} = k_{(\mathrm{LB})} * A^2 \qquad (\mathrm{A.2})$$

where *A* is the resolution of the digital rock, i.e. the physical size of a lattice grid (2.673 μm in this study).

Absolute permeability is an intrinsic property of a rock that is independent of the type of fluid. The single-phase simulations were conducted with several different values of fluid viscosity and body force to ensure the consistency of the results. When the fluid summation of velocity change in 1,000 steps difference was less than 2% for all cases, the simulations were assumed to have converged at that time. The absolute permeability results in various viscosity and body force conditions are shown in the table A.1.

| **kinematic viscosity (lattice-Boltzmann unit)** | **Body force (lattice-Boltzmann unit)** | **absolute permeability (Darcy)** |
|---|---|---|
| 0.155555 | 0.0001 | 1.3029 |
| 0.155555 | 0.0002 | 1.3025 |
| 0.310000 | 0.0001 | 1.3042 |
| 0.310000 | 0.0002 | 1.3038 |

Table A.1 single-phase simulation conditions and results

The absolute permeability of the Berea rock is 1.3034 ±0.001 Darcy. The absolute permeability value remains constant under various conditions, which demonstrates the accuracy and stability of the simulation. The result obtained from this simulation is slightly different from the result by the Dong and Blunt (2009), which gives the absolute permeability value of 1.193 Darcy. The difference might be due to the difference in size of digital rocks. Dong and Blunt used digital rock with dimension of 400x400x400 voxels with resolution of 5.345 μm (9.772 $mm^3$ in actual size), while we used digital rock with dimension of 400x400x400 voxels with resolution of 2.673 μm (1.222 $mm^3$ in actual size) is used. The dimension difference might have caused a slight change in the rock sample heterogeneity. In addition, Dong and Blunt applied Pore Network Model (PNM) to calculate the absolute permeability, while in this study, LBM simulation is used. Nonetheless, the absolute permeability value obtained is still in the same order as described by the paper.

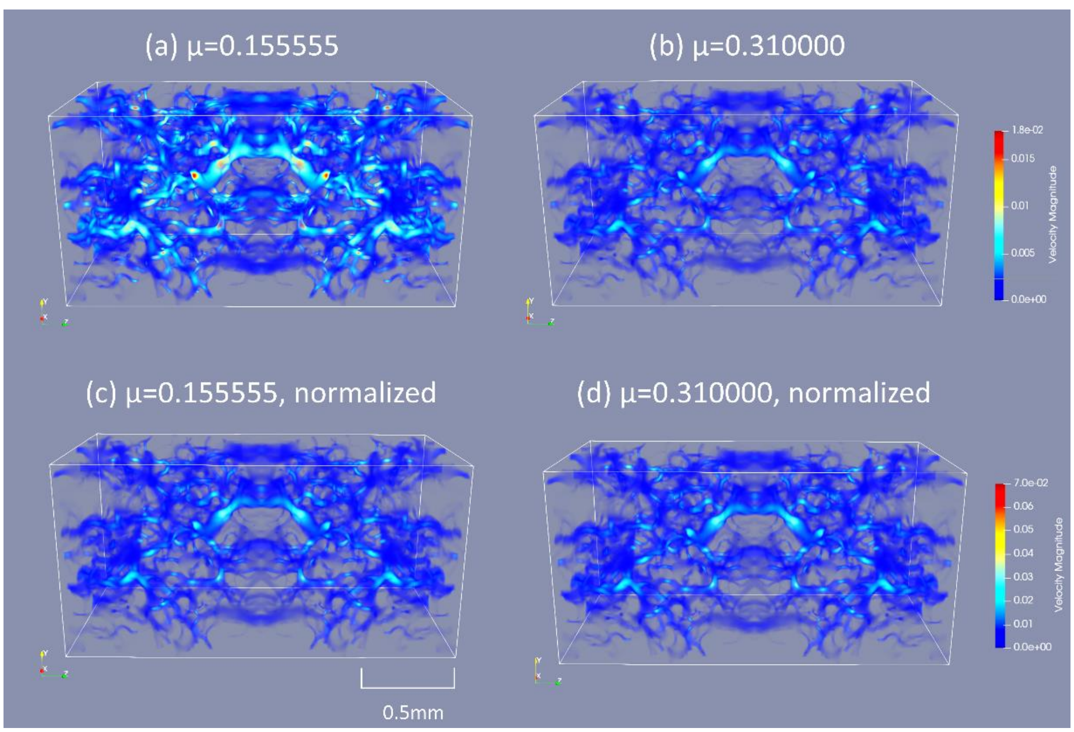


Fig. A. Velocity fields for single phase simulation at (a) μ = 0.155555 and (b) μ = 0.310000 and normalized velocity fields for single phase simulation at (c) μ = 0.155555 and (d) μ = 0.310000.

We show the velocity field of single-phase simulation for kinematic viscosity = 0.155555 and 0.310000 with equal body force of 0.0001 (Fig. A(a) and A(b)). The fluid velocity for simulation with fluid kinematic viscosity of 0.155555 nu_{LB} is significantly higher compared to the fluid kinematic viscosity of 0.310000 nu_{LB} case. This is because fluid average velocity is inversely proportional to viscosity. Thus, fluid velocity is not proportional to permeability, and must be normalized into dimensionless velocity field. Fig. A(c) and A(d) show the normalized fluid velocity field for both conditions. The normalization is done using the equation $U^{*} = \frac{U}{\Delta PL/\mu}$. Both figures show a relatively similar results, which indicate that a similar absolute permeability value is obtained from both conditions.

## B. Regression model of the $M$-$Ca$-$k_{nw}$ relationship

We created a regression model to generate an empirical equation that can be used to calculate $k_{nw}$ as a function of $M$ and log $Ca$ at 20% $S_{nw}$. A height map of our simulation results and the fitted polynomial regression curve is shown in Fig. B.

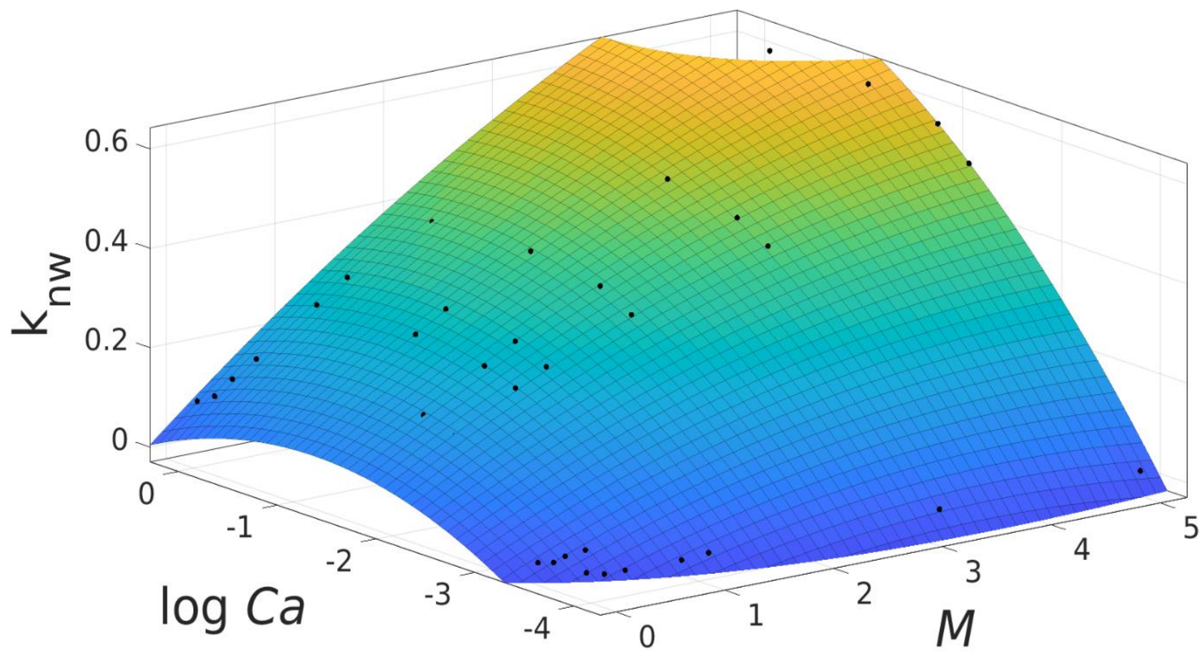


Fig. B. Nonwetting fluid relative permeability height map (dots) and the fitted polynomial regression curve.

Past research has shown that $k_{nw}$ can be estimated as a function of $M$ by using an equation with second-degree polynomial (equation 3 and 4 (Goldsmith & Mason, 1963)); thus, we chose a second polynomial equation for the regression towards the $M$ value. For the log $Ca$ value, we also set it as second-degree polynomial to prevent overfitting.

Based on our model, $k_{nw}$ can be calculated with the following formula:

$$k_{\mathrm{nw}} = 0.05983 + 0.1844\,M - 0.08714\,(\log Ca) - 0.009922\,M^2 + 0.0275M(\log Ca) - 0.03335\,(\log Ca)^2$$

Our model has an $R$-squared value of 0.9481 and a summed square of residuals value of 0.09871.

Because we created a color map diagram for only one saturation condition ($S_{nw}$ = 20%), we only created a regression model to calculate $k_{nw}$ based on $M$ and $Ca$ values for this saturation condition. Because the relative permeability increase with respect to saturation is not linear, we expect the regression model to be different for other saturation conditions. In the future, we plan to create more relative permeability color maps for various saturation conditions and create a four-dimensional log $M$–log $Ca$–$S_{nw}$–$k_{nw}$ graph to yield $k_{nw}$ estimates for all saturation conditions. Then, we will attempt to create a regression model to estimate $k_{nw}$ as a function of $M$, log $Ca$, and $S_{nw}$.

## References


Ahmadlouydarab, M., Liu, Z. S., & Feng, J. J. (2012). International Journal of Multiphase Flow Relative permeability for two-phase flow through corrugated tubes as model porous media. *International Journal of Multiphase Flow*, *47*, 85–93. http://dx.doi.org/10.1016/j.ijmultiphaseflow.2012.07.005

Ahrenholz, B., Tölke, J., Lehmann, P., Peters, A., Kaestner, A., Krafczyk, M., & Durner, W. (2008). Prediction of capillary hysteresis in a porous material using lattice-Boltzmann methods and comparison to experimental data and a morphological pore network model. *Advances in Water Resources*, *31*(9), 1151–1173. https://doi.org/10.1016/j.advwatres.2008.03.009

Amaefule, J. O., & Handy, L. L. (1982). The Effect of Interfacial Tensions on Relative Oil/Water Permeabilities of Consolidated Porous Media. *Society of Petroleum Engineers Journal*, *22*(03), 371–381. https://doi.org/10.2118/9783-PA

Asar, H., & Handy, L. L. (1989). Influence of interfacial tension on gas/oil relative permeability in a gas-condensate system. *Spe Reservoir Engng.*, *3*(1, Feb. 1989), 257–264. https://doi.org/10.2118/11740-pa

Bakhshian, S., Rabbani, H. S., & Shokri, N. (2021). Physics-Driven Investigation of Wettability Effects on Two-Phase Flow in Natural Porous Media: Recent Advances, New Insights, and Future Perspectives. *Transport in Porous Media*, *140*(1), 85–106. https://doi.org/10.1007/s11242-021-01597-z

Bear, J. (1975). Dynamics of Fluids in Porous Media: *Soil Science*, *120*(2), 162–163.

https://doi.org/10.1097/00010694-197508000-00022

Benson, S. M., Hingerl, F., Zuo, L., Krevor, S., Reynolds, C., Niu, B., Calvo, R., Niemi, A., Pini, R., Krevor, S., Reynolds, C., Niu, B., Calvo, R., & Niemi, A. (2015). Relative permeability for multi-phase flow in CO2 storage reservoirs. Part II: resolving fundamental issues and filling data gaps. *Global CCS Institute*, *December*, 1–52.

Bischofberger, I., Ramachandran, R., & Nagel, S. R. (2015). An island of stability in a sea of fingers: emergent large-scale features of the viscous flow instability. *ArXiv:1410.7623 [Physics]*. http://arxiv.org/abs/1410.7623

Burnside, N. M., & Naylor, M. (2014). International Journal of Greenhouse Gas Control Review and implications of relative permeability of CO 2 / brine systems and residual trapping of CO 2. *International Journal of Greenhouse Gas Control*, *23*, 1–11. https://doi.org/10.1016/j.ijggc.2014.01.013

Chen, C., & Zhang, D. (2010). Pore-scale simulation of density-driven convection in fractured porous media during geological CO2 sequestration. *Water Resources Research*, *46*(11). https://doi.org/https://doi.org/10.1029/2010WR009453

Chen, S., & Doolen, G. D. (1998). LATTICE BOLTZMANN METHOD FOR FLUID FLOWS. *Annual Review of Fluid Mechanics*, *30*(1), 329–364. https://doi.org/10.1146/annurev.fluid.30.1.329

Dong, H., & Blunt, M. J. (2009). Pore-network extraction from micro-computerized-tomography images. *Physical Review E*, *80*(3), 36307. https://doi.org/10.1103/PhysRevE.80.036307

Dou, Z., & Zhou, Z. F. (2013). Numerical study of non-uniqueness of the factors influencing relative permeability in heterogeneous porous media by lattice Boltzmann method. *International Journal of Heat and Fluid Flow*, *42*, 23–32. https://doi.org/10.1016/j.ijheatfluidflow.2013.01.020

Esmaeili, S., Modaresghazani, J., Sarma, H., Harding, T., & Maini, B. (2020). Effect of temperature on relative permeability – Role of viscosity ratio. *Fuel*, *278*. https://doi.org/10.1016/j.fuel.2020.118318

Fan, M., Dalton, L. E., McClure, J., Ripepi, N., Westman, E., Crandall, D., & Chen, C. (2019). Comprehensive study of the interactions between the critical dimensionless numbers associated with multiphase flow in 3D porous media. *Fuel*, *252*, 522–533. https://doi.org/10.1016/j.fuel.2019.04.098

Fulcher, R. A., Ertekin, T., & Stahl, C. D. (1985). Effect of Capillary Number and Its Constituents on Two-Phase Relative Permeability Curves. *JPT, Journal of Petroleum Technology*, *37*(2), 249–260. https://doi.org/10.2118/12170-PA

Goel, G., Abidoye, L. K., Chahar, B. R., & Das, D. B. (2016). Scale dependency of dynamic relative permeability–satuartion curves in relation with fluid viscosity and dynamic capillary pressure effect. *Environmental Fluid Mechanics*, *16*(5), 945–963. https://doi.org/10.1007/s10652-016-9459-y

Goldsmith, H. L., & Mason, S. G. (1963). The flow of suspensions through tubes. II. Single large bubbles. *Journal of Colloid Science*, *18*(3), 237–261. https://doi.org/10.1016/0095-8522(63)90015-1

Gudjonsdottir, M., Palsson, H., Eliasson, J., & Saevarsdottir, G. (2015). Calculation of relative permeabilities from field data and comparison to laboratory measurements. *Geothermics*, *54*, 1–9. https://doi.org/10.1016/j.geothermics.2014.10.004

Harbert, L. W. (1983). Low interfacial tension relative permeability. *Proceedings - SPE Annual Technical Conference and Exhibition*, *1983-Octob*, 2–9. https://doi.org/10.2523/12171-ms

Heins, R., Simjoo, M., Zitha, P. L., & Rossen, W. R. (2014). Oil Relative Permeability During Enhanced Oil Recovery by Foam Flooding. In *SPE Annual Technical Conference and Exhibition*. https://doi.org/10.2118/170810-MS

Honarpour, M., Koederitz, L., & Harvey, A. (2018). Relative Permeability of Petroleum Reservoirs. In *Relative Permeability of Petroleum Reservoirs*. https://doi.org/10.1201/9781351076326

Huang, H., & Lu, X. Y. (2009). Relative permeabilities and coupling effects in steady-state gas-liquid flow in porous media: A lattice Boltzmann study. *Physics of Fluids*, *21*(9). https://doi.org/10.1063/1.3225144

Huang, H., Sukop, M. C., & Lu, X.-Y. (2015). Rothman–Keller multiphase Lattice Boltzmann model. In *Multiphase Lattice Boltzmann Methods: Theory and Application* (pp. 94–135). https://doi.org/https://doi.org/10.1002/9781118971451.ch4

Huang, H., Wang, L., & Lu, X. Y. (2011). Evaluation of three lattice Boltzmann models for multiphase flows in porous media. *Computers and Mathematics with Applications*, *61*(12), 3606–3617. https://doi.org/10.1016/j.camwa.2010.06.034

Jeong, G. S., Lee, J., Ki, S., Huh, D. G., & Park, C. H. (2017). Effects of viscosity ratio, interfacial tension and flow rate on hysteric relative permeability of CO2/brine systems. *Energy*, *133*, 62–69. https://doi.org/10.1016/j.energy.2017.05.138

Jiang, F, & Tsuji, T. (2017). Estimation of three-phase relative permeability by simulating fluid dynamics directly on rock-microstructure images: ESTIMATION OF THREE-PHASE PERMEABILITY. *Water Resources Research*, *53*(1), 11–32. https://doi.org/10.1002/2016WR019098

Jiang, Fei, Liu, H., Chen, X., & Tsuji, T. (2022). A coupled LBM-DEM method for simulating the multiphase fluid-solid interaction problem. *Journal of Computational Physics*, *454*, 110963. https://doi.org/10.1016/j.jcp.2022.110963

Jiang, Fei, & Tsuji, T. (2014). Changes in pore geometry and relative permeability caused by carbonate precipitation in porous media. *Physical Review E*, *90*(5), 53306. https://doi.org/10.1103/PhysRevE.90.053306

Jiang, Fei, & Tsuji, T. (2016). Numerical investigations on the effect of initial state CO2 topology on capillary trapping efficiency. *International Journal of Greenhouse Gas Control*, *49*, 179–191. https://doi.org/10.1016/j.ijggc.2016.03.006

Jiang, Fei, Tsuji, T., & Hu, C. (2014). Elucidating the Role of Interfacial Tension for Hydrological Properties of Two-Phase Flow in Natural Sandstone by an Improved Lattice Boltzmann Method. *Transport in Porous Media*, *104*(1), 205–229. https://doi.org/10.1007/s11242-014-0329-0

Jiang, Fei, Yang, J., Boek, E., & Tsuji, T. (2021). Investigation of viscous coupling effects in three-phase flow by lattice Boltzmann direct simulation and machine learning technique. *Advances in Water Resources*, *147*, 103797. https://doi.org/10.1016/j.advwatres.2020.103797

Johnson, E. F., Bossler, D. P., & Bossler, V. O. N. (1959). Calculation of Relative Permeability from Displacement Experiments. *Transactions of the AIME*, *216*(01), 370–372. https://doi.org/10.2118/1023-G

Lefebvre du Prey, E. J. (1973). Factors Affecting Liquid-Liquid Relative Permeabilities of a Consolidated Porous Medium. *Society of Petroleum Engineers Journal*, *13*(01), 39–47. https://doi.org/10.2118/3039-PA

Lenormand, R., Touboul, E., & Zarcone, C. (1988). Numerical models and experiments on immiscible displacements in porous media. *Journal of Fluid Mechanics*, *189*, 165–187. https://doi.org/10.1017/S0022112088000953

Li, H., Pan, C., & Miller, C. T. (2005). Pore-scale investigation of viscous coupling effects for two-phase flow in porous media. *Physical Review E - Statistical, Nonlinear, and Soft Matter Physics*, *72*(2), 1–14. https://doi.org/10.1103/PhysRevE.72.026705

Li, X., Jiang, F., & Hu, C. (2016). Analysis of the accuracy and pressure oscillation of the lattice Boltzmann method for fluid–solid interactions. *Computers & Fluids*, *129*, 33–52. https://doi.org/10.1016/j.compfluid.2016.01.015

Mahmoudi, S., Mohammadzadeh, O., Hashemi, A., & Kord, S. (2017). Pore-scale numerical modeling of relative permeability curves for CO2–oil fluid system with an application in immiscible CO2 flooding. *Journal of Petroleum Exploration and Production Technology*, *7*(1), 235–249. https://doi.org/10.1007/s13202-016-0256-4

McDougall, S. R., Salino, P. A., & Sorbie, K. S. (2007). *The Effect of Interfacial Tension Upon Gas-Oil Relative Permeability Measurements: Interpretation Using Pore-Scale Models*. https://doi.org/10.2523/38920-ms

Mu'min, G. F., Kawaguchi, T. (川口 達也 ), & Saito, T. (齊藤 卓志 ). (2021). Droplet breakup of a high-viscosity-ratio system in a nonuniform temperature field under laser irradiation. *Physics of Fluids*, *33*(7), 73108. https://doi.org/10.1063/5.0055235

Nekouei, M., & Vanapalli, S. A. (2017). Volume-of-fluid simulations in microfluidic T-junction devices: Influence of viscosity ratio on droplet size. *Physics of Fluids*, *29*(3), 32007. https://doi.org/10.1063/1.4978801

Niibori, Y., Ahn, J., & Mimura, H. (2011). Uncertainty of Relative Permeability to Describe Two-Phase Flow in Geological Disposal System. *Nuclear Technology*, *175*(3), 641–651. https://doi.org/10.13182/NT11-A12512

Odeh, A. S. (1959). Effect of Viscosity Ratio on Relative Permeability (includes associated paper 1496-G). *Transactions of the AIME*, *216*(01), 346–353. https://doi.org/10.2118/1189-G

Øren, P. E., & Bakke, S. (2003). Reconstruction of Berea sandstone and pore-scale modelling of wettability effects. *Journal of Petroleum Science and Engineering*, *39*(3–4), 177–199.

https://doi.org/10.1016/S0920-4105(03)00062-7

Rabbani, H. S., Joekar-Niasar, V., Pak, T., & Shokri, N. (2017). New insights on the complex dynamics of two-phase flow in porous media under intermediate-wet conditions. *Scientific Reports*, *7*(1), 4584. https://doi.org/10.1038/s41598-017-04545-4

Ramstad, T., Idowu, N., Nardi, C., & Øren, P.-E. (2012). Relative Permeability Calculations from Two-Phase Flow Simulations Directly on Digital Images of Porous Rocks. *Transport in Porous Media*, *94*(2), 487–504. https://doi.org/10.1007/s11242-011-9877-8

Ramstad, T., Øren, P. E., & Bakke, S. (2010). Simulation of two-phase flow in Reservoir rocks using a lattice Boltzmann method. *SPE Journal*, *15*(4), 923–933. https://doi.org/10.2118/124617-pa

Shad, S., Gates, I. D., & Maini, B. B. (2008). Experimental study of heavy oil-water flow structure effects on relative permeabilities in a fracture filled with heavy oil. *Society of Petroleum Engineers - International Thermal Operations and Heavy Oil Symposium, ITOHOS 2008 - "Heavy Oil: Integrating the Pieces," 2*, 690–701. https://doi.org/10.2118/117644-ms

Shen, P., Zhu, B., Li, X. Bin, & Wu, Y. S. (2010). An Experimental Study of the Influence of Interfacial Tension onWater-Oil Two-Phase Relative Permeability. *Transport in Porous Media*, *85*(2), 505–520. https://doi.org/10.1007/s11242-010-9575-y

Singh, S., Jiang, F., & Tsuji, T. (2017). Influence of Slip Flow at Fluid-solid Interface upon Permeability of Natural Rock. *Energy Procedia*, *114*, 3572–3577. https://doi.org/10.1016/j.egypro.2017.03.1487

Stone, H. A. (1994). Dynamics of Drop Deformation and Breakup in Viscous Fluids. *Annual Review of Fluid Mechanics*, *26*(1), 65–102. https://doi.org/10.1146/annurev.fl.26.010194.000433

Succi, S., Sbragaglia, M., & Ubertini, S. (2010). Lattice Boltzmann Method. *Scholarpedia*, *5*(5), 9507. https://doi.org/10.4249/scholarpedia.9507

Tölke, J., Freudiger, S., & Krafczyk, M. (2006). An adaptive scheme using hierarchical grids for lattice Boltzmann multi-phase flow simulations. *Computers & Fluids*, *35*(8), 820–830. https://doi.org/https://doi.org/10.1016/j.compfluid.2005.08.010

Tsuji, T., Jiang, F., & Christensen, K. T. (2016). Characterization of immiscible fluid displacement processes with various capillary numbers and viscosity ratios in 3D natural sandstone. *Advances in Water Resources*, *95*, 3–15. https://doi.org/10.1016/j.advwatres.2016.03.005

Vafai, K. (2000). *Handbook of Porous Media*. Marcel Dekker, Inc.

Wu, Q., & Wang, J. (2020). A thermo-hydro-mechanical coupling analysis for the contaminant transport in a bentonite barrier with variable saturation. *Water (Switzerland)*, *12*(11), 1–23. https://doi.org/10.3390/w12113114

Yang, J., & Boek, E. S. (2013). A comparison study of multi-component Lattice Boltzmann models for flow in porous media applications. *Computers and Mathematics with Applications*, *65*(6), 882–890. https://doi.org/10.1016/j.camwa.2012.11.022

Yiantsios, S. G., & Higgins, B. G. (1988). Numerical solution of eigenvalue problems using the compound matrix method. *Journal of Computational Physics*, *74*(1), 25–40. https://doi.org/10.1016/0021-9991(88)90066-6

Yih, C. S. (1967). Instability due to viscosity stratification. *Journal of Fluid Mechanics*, *27*(2), 337–352. https://doi.org/10.1017/S0022112067000357

Yiotis, A. G., Psihogios, J., Kainourgiakis, M. E., Papaioannou, A., & Stubos, A. K. (2007). A lattice Boltzmann study of viscous coupling effects in immiscible two-phase flow in porous media. *Colloids and Surfaces A: Physicochemical and Engineering Aspects*, *300*(1-2 SPEC. ISS.), 35–49. https://doi.org/10.1016/j.colsurfa.2006.12.045

Zhang, Y., Jiang, F., & Tsuji, T. (2022). Influence of pore space heterogeneity on mineral dissolution and permeability evolution investigated using lattice Boltzmann method. *Chemical Engineering Science*, *247*, 117048. https://doi.org/10.1016/j.ces.2021.117048

Zhao, H., Ning, Z., Kang, Q., Chen, L., & Zhao, T. (2017). Relative permeability of two immiscible fluids flowing through porous media determined by lattice Boltzmann method. *International Communications in Heat and Mass Transfer*, *85*(May), 53–61. https://doi.org/10.1016/j.icheatmasstransfer.2017.04.020

Zheng, X., Mahabadi, N., Yun, T. S., & Jang, J. (2017). Effect of capillary and viscous force on CO2 saturation and invasion pattern in the microfluidic chip. *Journal of Geophysical Research: Solid Earth*, *122*(3), 1634–1647. https://doi.org/https://doi.org/10.1002/2016JB013908

## Figure Caption

Fig. 1. Berea sandstone digital rock model: (a) core form and (b) mirrored form.

Fig. 2. Relative permeability curves as a function of $M$ at constant log $Ca = -0.25 \pm 0.1$ for $M = 0.1$–5: (a) nonwetting fluid relative permeability ($k_{nw}$) curve and (b) wetting fluid relative permeability ($k_w$) curve.

Fig. 3. Two-dimensional slice showing the distributions of nonwetting fluid (red), wetting fluid (green), and solid rock (black) at various values of $M$ and $S_{nw}$.

Fig. 4. Evolution of the number of clusters of nonwetting fluid at $M = 1$ and $M = 5$, with $S_{nw} = 20\%$ and log $Ca = -0.25 \pm 0.1$.

Fig. 5. Two-dimensional slice showing the distributions of nonwetting (red), wetting fluid (green), and solid rock (black) at (a) $M = 1$ and (b) $M = 5$ at 20% $S_{nw}$. These images show a portion of the slice illustrated in Fig. 3.

Fig. 6. Normalized velocity fields for the nonwetting fluid in a two-phase simulation with (a) $M = 1$ and (b) $M = 5$, at log $Ca = -0.25 \pm 0.1$ and $S_{nw} = 20\%$.

Fig. 7. Relative permeability curves for the nonwetting ($k_{nw}$, green) and wetting fluids ($k_w$, blue) for log $Ca = -0.25$ to $-3.5$ with $M = 1$.

Fig. 8. Relative permeability map of the nonwetting fluid for (a) log $M = -1.02$ to 0.70 and log $Ca = -4.00$ to 0.00, and (b) log $M = -1.02$ to 0.00 and log $Ca = -4.00$ to $-1.00$. The dots indicate the *Ca*–*M* conditions used for LBM simulation.

Fig. A. Velocity fields for single phase simulation at (a) $\mu = 0.155555$ and (b) $\mu = 0.310000$ and normalized velocity fields for single phase simulation at (c) $\mu = 0.155555$ and (d) $\mu = 0.310000$.

Fig. B. Nonwetting fluid relative permeability height map (dots) and the fitted polynomial regression curve.